A young solar twin in the Rosette cluster NGC 2244 line of sight

Jeremy M. Huber,[1]* John F. Kielkopf,[2]* Matthew Mengel,[3] Bradley D. Carter,[3]
Gary J. Ferland[4] and Frank O. Clark[2]

[1]*Department of Mathematics and Physics, Thomas More College, 333 Thomas More Parkway, Crestview Hills, KY 41017, USA*
[2]*Department of Physics and Astronomy, University of Louisville, Louisville, KY 40292, USA*
[3]*Astrophysics Group, Computational Engineering and Science Research Centre, University of Southern Queensland, Toowoomba, Queensland 4350, Australia*
[4]*Department of Physics and Astronomy, University of Kentucky, Lexington, KY 40506, USA*

ABSTRACT

Based on prior precision photometry and cluster age analysis, the bright star GSC 00154−01819 is a possible young pre-main sequence member of the Rosette cluster, NGC 2244. As part of a comprehensive study of the large-scale structure of the Rosette and its excitation by the cluster stars, we noted this star as a potential backlight for a probe of the interstellar medium and extinction along the sight line towards a distinctive nebular feature projected on to the cluster centre. New high-resolution spectra of the star were taken with the University College London Echelle Spectrograph of the AAT. They reveal that rather than being a reddened spectral type B or A star within the Mon OB2 association, it is a nearby, largely unreddened, solar twin of spectral type G2V less than 180 Myr old. It is about 219 pc from the Sun with a barycentric radial velocity of $+14.35 \pm 1.99 \, \mathrm{km \, s^{-1}}$. The spectrum of the Rosette behind it and along this line of sight shows a barycentric radial velocity of $+26.0 \pm 2.4 \, \mathrm{km \, s^{-1}}$ in Hα, and a full width at half-maximum velocity dispersion of $61.94 \pm 1.38 \, \mathrm{km \, s^{-1}}$.

Key words: stars: distances – stars: solar-type – H II regions.

1 INTRODUCTION

The Rosette nebula is a nearby (1.6 kpc) star-forming H II region driven by a central cluster of OB stars, NGC 2244 (Román-Zúñiga & Lada 2008a,b). At four times the distance of the Orion nebula, it subtends nearly 2° on the sky. The physical processes and even the three-dimensional structure of this region are not fully understood, and we are applying multispectral imaging together with CLOUDY (Ferland et al. 2017) code for 3D modelling to investigate the processes that are responsible for its current state. In spite of its faintness and large angular size, this region is rich in finely structured 'elephant trunk' globules, dense concentrations of dust which are generally seen as long strands in absorption against the background gas. A similar ridge condensation, not evident in absorption, occupies a distinctive location as shown by the green and red streak at the centre of the nebula in Fig. 1. Isolated without connection to other diffuse emission, it is not seen in the visible spectrum where dust would scatter light from a star such as HD 46150. Therefore, it is likely in the foreground, along the line of sight to the central cluster, affording a unique opportunity to explore its chemistry through interstellar absorption line diagnostics by observing more distant cluster members.

This object was initially identified in image data from the Midcourse Space Experiment (Kraemer et al. 2003) as anomalously bright at 14.7 and 21.3 μm compared to the other familiar features that are distinguished by their strong absorption of the Hα emission from the nebula. It was also recently detected in the WISE W4 (22 μm) band, where it appears distinctively in the composite of WISE W4 and W3 (12 μm) data with our Hα data shown in Fig. 1. The ridge-like arc of 25 μm emission is within 2 arcmin (1 pc projected on the distance of NGC 2244) of HD 46150, one of the O-stars of the cluster thought to excite the visible emission of the Rosette. This star's radiation field could produce the observed IR emission through thermal equilibrium of the dust. While the mid-IR emission from the usual elephant trunks in the Rosette has been identified as coming from dust carriers, there are problems with this interpretation for the anomalous ridge, given its apparent proximity to the star. In order to have been stable for the lifetime of HD 46150, the anomalous ridge would have to be very massive, and should contain molecular material. Alternatively, it may be a recently formed transient, or a foreground feature heated by an embedded star.

Since the bright star HD 46150 exhibits strong diffuse interstellar bands (Walker 1963; Weselak et al. 2008; Krełowski, Galazutdinov & Kołos 2011; ESO 2015), we expect that line-of-sight absorption spectroscopy would provide a unique opportunity to probe a cloud of dust and molecular gas in an environment being modelled for its detailed physical processes. Fortunately, there is one star

* E-mail: jhuber42@gmail.com (JMH); kielkopf@louisville.edu (JFK)
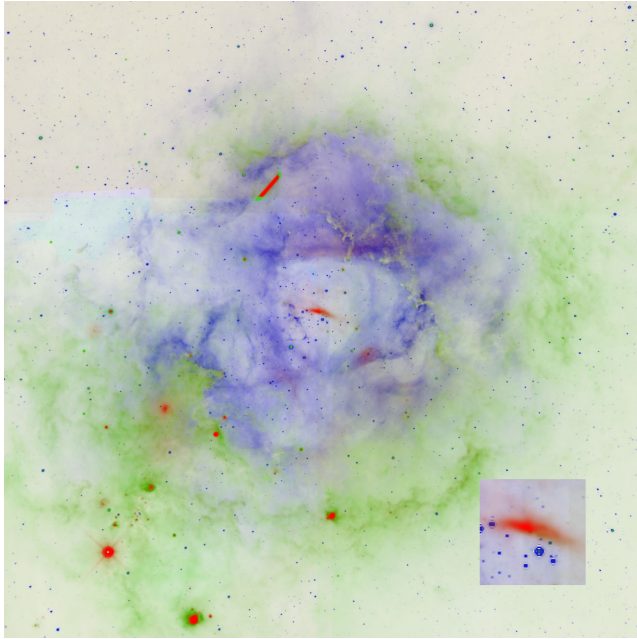
Figure 1. Rosette nebula in a $2° \times 2°$ field surrounding HD 46150 in NGC 2244. Blue: Hα; green: WISE W3 (12 µm); red: WISE W4 (22 µm). The bright streak near the top of the optical nebula is an artefact in the WISE data. The inset lower right is a 6.6 arcmin $\times$ 6.6 arcmin enlarged view of the centre.

Figure 2. Finder chart for GSC 00154−01819. The 20 arcmin field shown is from the red Digital Sky Survey, and is centred on HD 46150, an O5V star responsible for exciting the nebular emission. Other bright stars in NGC 2244 are marked, along with the target star. The anomalous ridge is not visible in optical images.

bright enough for high resolution spectroscopy that appears to be at the edge of the anomalous ridge in the multispectral data cube. To date, this source has been identified as GSC 00154−01819, a $V = 11.6$ mag source classified as a type A star that has not been studied previously, other than to note its association with the central cluster (Wang et al. 2008). A finder chart for this star is shown in Fig. 2. The hot O5V star HD 46150 is the much brighter ($V = 7.78$ mag) source located 1.42 arcmin to the southwest.

High-resolution spectra of stars in the neighbourhood of the Rosette would reveal the interstellar cloud motions and composition along a critical central sight line into the centre of the Rosette nebula, as well as interstellar absorption within it. Also, if the anomalous ridge is in front of the star, then the data will assist in identifying the nature of this unusual object.

2 CLUSTER MEMBERSHIP

There have been several studies of the membership of stars in the Rosette nebula cluster NGC 2244 intended to distinguish foreground and background stars from those actually located within a reasonable cluster boundary. Table 1 summarizes the conclusions for the star of interest. The cluster's distance exceeds the precision of the *Gaia* DR1 release (Gaia Collaboration 2016) for all but the brightest sources. Without high-resolution spectra or precision parallax determinations, there are two other tools available for determining cluster membership: proper motion and the relationships of star colours and magnitudes. The earliest precision proper motion measurements were compiled by van Schewick (1958), including our target star within the cluster. Subsequently, Johnson (1962) undertook photoelectric photometry and on that basis decided that the star was not a cluster member, presumably using selection criteria on a V versus $B − V$ magnitude–colour diagram.

Ogura & Ishida (1981) used three-colour UBV photometry with both photoelectric and photographic observations to understand
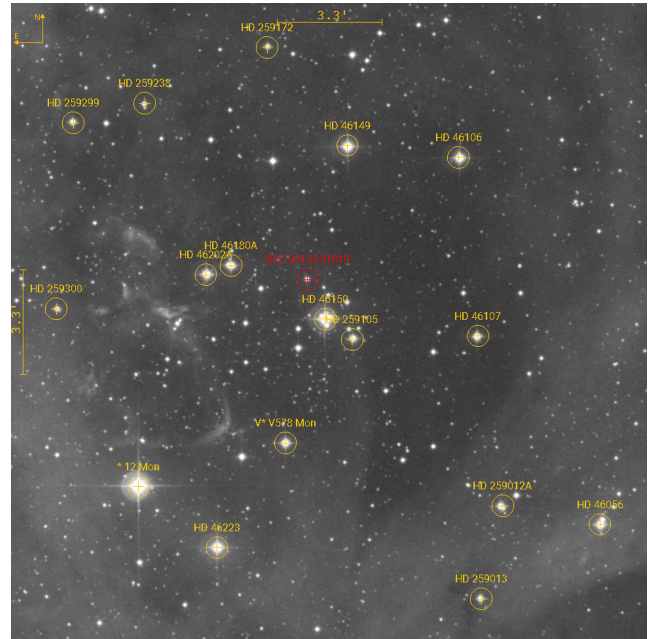
Table 1. NGC 2244 cluster membership for GSC 00154−01819.

Identifier	Cluster membership Methods[a]	Selection[b]
VS 31[c]	PM	Y?
JOHN 26[d]	CM	N
OI NGC 2244 181[e]	CM	N
BC 566[f]	CM	Y?
PS 2076[g]	PM	0.0
CDZ 88[h]	PM	0.70
WTF Main 429[i]	CM	Y

[a]Proper motion (PM); color and magnitude (CM); radial velocity (RV); [b]Member (Y), non-member (N), or probability (0 - 1);[c]van Schewick (1958); [d]Johnson (1962);[e]Ogura & Ishida (1981); [f]Berghöfer & Christian (2002); [g]Park & Sung (2002); [h]Chen et al. (2007);[i]Wang et al. (2008).

the colour excess $E(B − V)$ and total-to-selective extinction ratio $R = A_V/E(B − V)$ given an apparently anomalous value of R for NGC 2244. They analysed $P = V − R(B − V)$ versus $Q = (U − B) − X(B − V)$ where $X = E_{U−B}/E_{B−V}$, and adopted values of $E_{B−V} = 0.47$ and $X = 0.73$, leading to a best fit for $R = 3.2 \pm 0.2$ for the cluster. With that, they compared the extinction-free magnitude P to the reddening-free colour Q to identify stars that are brighter and redder than expected for a zero-age main-sequence cluster member. Our target, their star 181, is not a cluster member on this basis, and is identified as a foreground star.

Berghöfer & Christian (2002) also constructed a V versus $B − V$ colour magnitude diagram of NGC 2244 in the course of their study of the X-ray properties of the cluster stars. From this they

identified the pre-main sequence stars known to be active with strong X-ray and Hα emission. They make no specific note of our target, their star 56, in the paper or the associated table, other than to report the measurements of B (12.28), V (11.61), R (11.01), I (10.74), and Hα (11.15) magnitudes. However, their fig. 6 illustrates a V versus $B - V$ colour–magnitude diagram on which star 56 falls mid-way between the zero age main-sequence (ZAMS) for the lower and upper reddening limits of $E_{B-V} = 0.38$ and $E_{B-V} = 0.85$. On this basis the star would be a candidate for cluster membership.

In the same year, Park & Sung (2002) also reported new UBVI and Hα photometry. Based on their new data, they adopt a colour excess ratio of $E_{U-B}/E_{B-V} = 0.72$ to find $E(B - V) = 0.47 \pm 0.04$ from 28 members of NGC 2244 brighter than $V = 14$. They consider differences in the colour excess ratio found by other authors, and some differences in reddening across the cluster, to construct colour–magnitude diagrams of V versus $V - I$, $B - V$, $U - B$, and Hα compared to ZAMS relations. They also incorporated proper-motion data and spectral types that had previously been measured and found $E(V - I)/E(B - V) = 1.27 \pm 0.06$, $R_V = 3.2 \pm 0.2$, and a distance modulus $V_0 - M_V = 11.1$ for probable members of the cluster. This distance modulus thus yields a distance of 1.7 kpc to the cluster. They did not single out our target, their star 207, as distinctive, although plotted on their fig. 8 of I versus $V - I$ the star would be brighter and less red than most stars of the cluster. The star could, in this context, be either a bright star with mass in excess of 2.5 M$_\odot$ in or near the cluster, or a fainter foreground star of solar mass. They do not assign a spectral type, but they do give a 0 per cent probability for cluster membership, and a membership quality assessment of 10/10 based on proper motion. The binary variable star V578 Mon in the Rosette has a somewhat smaller spectroscopic distance of 1.39 ± 0.1 kpc (Hensberge, Pavlovski & Verschueren 2000).

Chen, de Grijs & Zhao (2007) studied proper motions of the NGC 2244 field, identifying GSC 00154−01819 as star 88 in their catalogue. They find a higher membership probability of 70 per cent in their study, distinguished by a comprehensive analysis of the statistics of proper motion distributions.

Wang et al. (2008) used *Chandra* to study the stellar population of NGC 2244. They identified over 900 X-ray sources, and 77 per cent of them had optical or near-infrared stellar counterparts. GSC 00154−01819 is star 429 in their main catalogue which included J, H, and K photometry. In their fig. 6 of J versus J–H it falls among a few exceptionally bright stars slightly to the right (red) side of the ZAMS for B5V, and almost exactly on the 2 Myr isochrone for pre-main sequence stars. Thus their data suggest that the star is a cluster member, and is young, hot, and ideal source for our use.

3 ARCHIVAL STELLAR DATA

Table 2 summarizes the previously known information about the target of interest, GSC 00154−01819.

4 NEW SPECTROSCOPIC OBSERVATIONS

There are few public data on spectra of stars in NGC 2244, or on stars that are not cluster members but lie along the line of sight to the region (Román-Zúñiga & Lada 2008b,a). A dissertation on the cluster stars that is widely referenced (Verschueren 1991) for low resolution spectra is not available to us, but published work based on it (Hensberge, Vrancken & Verschueren 1998; Park & Sung 2002)

Table 2. Archival data on GSC 00154−01819.[a]

Common identifications	
GSC 00154 − 01819	
2MASS J06315775 + 0457496[b]	
USNO-B1.0 0949 − 00095001	
WISE J063157.75 + 045749.6	
Spatial parameters	
Right ascension	06^{h}31^{m}57.754^s ICRS (J2000)
Declination	+04°57′49.67″ ICRS (J2000)
Proper motion	3.412 $\pm$ 1.576 mas yr^{-1}
Proper motion	−13.231 $\pm$ 0.690 mas yr^{-1}
Parallax	Unknown
Distance	Unknown
Radial velocity	Unknown
Photometry	
Spectral type	A7/A8
U	12.33
B	12.185
V	11.565
R	11.01
I	10.85
J	10.409 $\pm$ 0.024
H	10.131 $\pm$ 0.021
K	10.076 $\pm$ 0.023

[a] Wenger et al. (2000).
[b] Young stellar object candidate.

suggest that the star of interest to us here was not included. A search of the ESO archive as of 2015 December 15, showed only a few nearby stars with echelle spectra in the visible and near-infrared were available.

Consequently, we requested a service run to obtain spectra of GSC 00154−01819 with the University College London Echelle Spectrograph (UCLES) on the Anglo-Australian 3.9 m telescope, since it offers high resolution and broad wavelength coverage with stability and precision suitable for radial velocity and line profile measurements (Diego et al. 1990; Tinney et al. 2001; Wright 2015).

The data were acquired with the 31.6 groove mm^{-1} echelle grating set for a central wavelength of 6050 Å in the 94th echelle order, with the E2V CCD camera. The 1 arcsec slit projects to about 4 pixels on the detector in the dispersion direction. Perpendicular to the width of the slit, an aperture mask limits sky background and eliminates blending across orders, projecting on a scale of 0.16 arcsec pixel^{-1} which are binned during acquisition 2:1 into the output data on a scale of 0.32 arcsec pixel^{-1}. The Balmer Hα line appears in both orders $m = 86$ and 87. In the 86th order the wavelength scale is nominally 0.0372 Å pixel^{-1}. The 4-pixel slit width thus limits the resolution to about 44 000 at Hα. While higher resolution can be obtained with a narrower slit, this is accompanied by a considerable loss of light in 1.5 arcsec median seeing since the slit clips the point-spread function (PSF) in the telescope focal plane. In the orthogonal direction, the aperture mask also limits the light that would be detected from the field near the star. For our data, this is equivalent to ± 5 pixels in the focal plane above and below the limits of the star's PSF-widened spectrum. That is, the spectra show the star and a small sample of the nebula less than ± 2 arcsec to either side of the stellar PSF. Three 1200-s exposures on the star were taken for a total of 1 h on the star, along with Th–Ar spectral and quartz lamp continuum calibrations.

A summary of the science data spectral files provided by the observing run is in Table 3.

**Table 3.** Spectra of GSC 00154−01819 with the AAT UCLES from Program UC 208.

Anglo-Australian telescope and spectrograph	
Observatory altitude	1164 m
Observatory latitude	−31.277 04°
Observatory longitude	149.0661°
Telescope	3.9 m AAT
Top end focal ratio	f/36
Spectrograph	UCLES with wide collimator
Grating	31.6 groove mm^{-1} echelle
Central λ	6050.0 Å in order 94
Detector	EEV2
Detector size	2048 × 4096
Binning	$x = 2{:}1, y = 1{:}1$
Spectral image size	2750 × 1044 with overscan
Detector pixel	13.5 μm square
Slit width	0.97 arcsec
Plate scale	Binned 2:1 to 0.32 arcsec pixel^{-1}
Dispersion	0.0384 Å pixel^{-1} in order 87 (H α)

UCLES spectra of GSC 00154−01819 on UT 2015:02:03		
UT mid	Mean zenith distance (deg)	Exposure (s)
10:18:36	42.5	1200
10:41:52	39.1	1200
11:03:12	37.5	1200
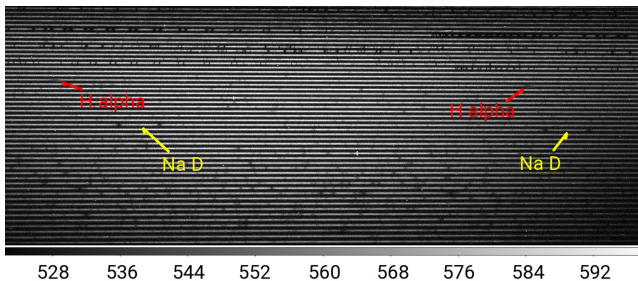
Figure 3. An echelle spectrum of GSC 00154−01819. The FITS science image has been rotated 90° and transposed so that dispersion is horizontal with wavelength increasing to the right. Lower orders (longer wavelength) are at the top. The Na D (orders 96 and 97) and H α (orders 86 and 87) lines are indicated. H β, near the lower edge, is in order 117.

5 REDUCTION OF THE SPECTRAL DATA

The three spectra that were obtained had a total exposure time of 3600 s, sufficient to provide a high-resolution spectrum of the star once they were calibrated in wavelength and combined into a single data set. File 23, one of the three raw images, is reproduced in a linear grey-scale display in Fig. 3. From this image alone it is apparent that the star is not an early spectral type. The spectrum includes the faint background nebula, airglow emission lines, and the telluric O_2 system that is obvious as a pattern across the lowest orders of the cross-dispersed spectrum. Th–Ar spectra in separate exposures provided a first pass at wavelength calibration (Ryder 2000; ESO 2017). Current best laboratory wavelengths are available from a critical compilation of Lovis & Pepe (2007) based on precision measurements and transition identification by Palmer and Engleman (Palmer & Engleman 1983). However, the light path for an emission source may differ sufficiently for systematic small wavelength shifts to propagate through to the analysed stellar spectra. Given a preliminary wavelength calibration based on these references, the USQ processing pipeline [based on the ESPRIT software package Donati et al. (1997)] did flat-field, order extraction,

GSC 00154 01819 UCLES Spectrum
Telluric Model Comparison
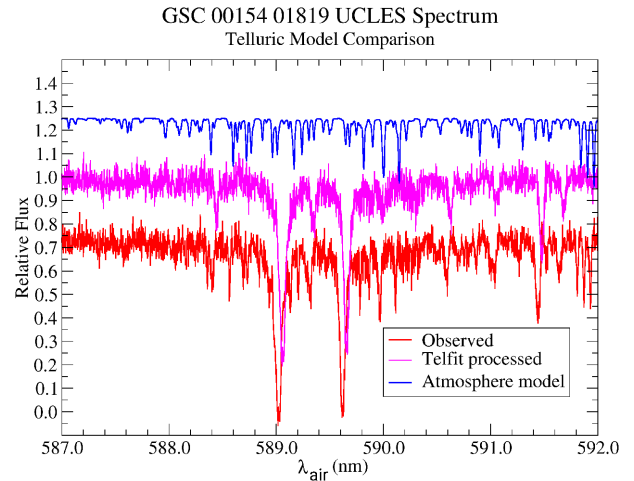
Figure 4. The Na D line region of the spectrum of GSC 00154−01819 from Telfit processing. The observed spectrum, a telluric best-fitting model, and the cleaned spectrum with telluric lines removed are shown displaced for clarity.

systematics correction in flux, and merged separate spectra orders into a single contiguous data set. The instrumental wavelength shifts from one image to another were found to be to negligible (Murphy et al. 2007) compared to the line widths and pixel spacing, and we combined the UCLES data from the three exposures into one sorted by wavelength.

These data were then resampled by interpolation on a linear mesh of 0.025 Å. This increment corresponds to a Δv in radial velocity of 1.25 km s^{-1}, and it does not degrade the pixel-limited resolution of the spectrograph in the regions of interest. To refine the wavelength calibration of the resampled spectrum, we used the PYTHON Telfit package (Gullikson, Dodson-Robinson & Kraus 2014). Telfit employs the Line-By-Line Radiative Transfer Model (Clough, Iacono & Moncet 2014) and the HITRAN data base (Gordon et al. 2016) to compute the absorption spectrum of Earth's atmosphere. It identifies telluric lines in the stellar spectrum, shifts the stellar spectrum to match the air wavelength of the known telluric standards, and removes the telluric lines to produce a new clean spectrum on a precise wavelength scale that is largely free of absorption lines from Earth's atmosphere. Telfit has been validated as an alternative for telluric standard star observations to correct for and remove telluric lines in near-infrared and optical stellar spectra. Its use of HITRAN, which is tied to laboratory spectra of major atmospheric constituents, accurately calibrates the stellar spectrum to geocentric standards on an absolute wavelength scale using the same light path as the star of interest (Gullikson et al. 2014).

Fig. 4 compares the observed spectrum to the Telfit processed spectra. We note that Telfit identified the telluric lines correctly, and found a systematic shift between those standards and the Th–Ar calibration from the preliminary reduction of the UCLES data. Telfit also found an instrumental resolution of 44 759 taken over the entire spectrum, and using that removed the atmospheric lines by modelling their contribution to the observed spectrum. The narrowness of the atmospheric lines is obvious in the figure, and with instrumental broadening their contributions to the observed spectrum in the region shown are subtle but significant. Subsequent analysis uses the clean spectrum after Telfit processing with telluric lines removed and wavelength calibration from the atmospheric standards.

6 COMPARISON TO STELLAR SPECTRUM MODELS

The recent PHOENIX library of stellar high resolution synthetic spectrum models provides a reference for unambiguously determining the stellar spectrum type given a high resolution spectrum (Husser et al. 2013). This physics-based self-consistent computation develops LTE (local thermodynamic equilibrium) model atmospheres with micro-turbulence, and includes elemental abundances, energy levels, and transition probabilities in model spectra at a resolution of $R = \lambda/\Delta\lambda = 500\,000$ for the optical and near-infrared. It uses more recent solar abundances than those of the Kurucz ATLAS9 (Kurucz 1970; Castelli & Kurucz 2003; Sbordone et al. 2004) model, while generating spectra that agree with those of that lower resolution atlas. The PHOENIX spectra produce more accurate line shapes at high resolution. However, because PHOENIX uses synthetic spectra, some absorption lines present in the observed spectra are missing in its models, while they are present in the AT-LAS9 model. This PHOENIX library has a grid of surface gravities from $\log(g) = -0.5$ to $\log(g) = 4.0$ with LTE surface temperatures from 2300 to 12 000 K, thus spanning the zero-age main sequence of spectral types of all but the hottest stars. Computed spectra are available in FITS data files that specify the LTE temperature, surface gravity [$\log(g)$ in cm s^{-2}], metallicity [$\log$ (metals/H) relative to solar] and α-element abundance enhancement. Since these are self-consistent stellar models, the library parameters also include microturbulent velocities for LTE, molecular, and non-LTE lines (km s^{-1}), stellar mass (grams), stellar radius (cm), and stellar luminosity (erg s^{-1}).

To identify the spectral type, we compared the clean spectrum to the model spectra in this grid. Small differences in $\log(g)$ and T_{eff} affect the shape and depth of lines in the Mg triplet region (5150–5120 Å), the Na D lines (5890 Å), and the Hα line (6563 Å) in distinctive ways. The dependence on α-process element abundances affects the strength of lines selectively. We found the nearest best-fitting grid spectrum was one with $\log(g) = 4.5$, $T_{\mathrm{eff}} = 5800$, and solar metallicity and α. For reference the surface gravity of the Sun is $2.74232 \times 10^4 \pm 7.9$ cm s^{-2}, or $\log(g) = 4.43$ cm s^{-2}, and its LTE temperature is $T_{\mathrm{eff}} = 5771.8 \pm 0.7$ K (Pecaut & Mamajek 2013; Mamajek 2015). Since the grid spacing is 100 K in T_{eff} and 0.5 in $\log(g)$, some additional refinement in the selection may be possible by interpolating the grid when higher signal-to-noise ratio spectra are available.

The stellar spectra in the PHOENIX model are computed with vacuum wavelengths, and without stellar rotation. Since the observed spectra are calibrated as wavelengths in air, it is necessary to convert back and forth between the two systems. Utilities in the PyAstronomy Library use the index of refraction of air computed with Edlen's method to transform entire spectral files as needed (Edlén 1966; Morton 1991; The PyA Group 2017). We work with vacuum wavelengths to determine the radial velocities by comparison to the PHOENIX model spectra.

We also have to broaden the PHOENIX model spectra to account for the rotation of the star. This is done with the PyAstronomy Library 'rotBroad' function, which uses the PYTHON NUMPY library to convolve a rotational Doppler profile with the model stellar spectrum and generate a new model representing a rotating star of that type. The broadening function implements Gray's method of treating the effect of stellar rotation on a spectrum dependent on two parameters, the line-of-sight equatorial surface velocity $v\sin(i)$, and a linear limb-darkening coefficient ϵ (Carroll 1933; Collins & Truax 1995; Reiners & Schmitt 2002; Gray 2008). At low rotational
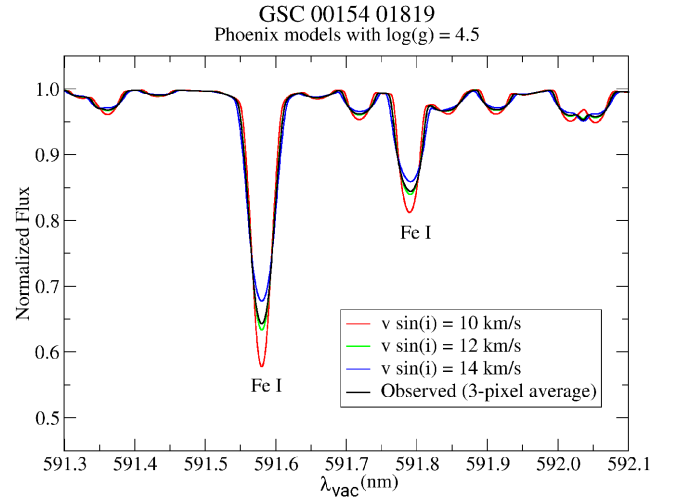

Figure 5. The spectrum of GSC 00154−01819 with telluric lines removed compared to rotationally broadened PHOENIX models at $T_{\mathrm{eff}} = 5800$ K with limb-darkening coefficient $\epsilon = 0.5$. Models with $\epsilon = 0.5 \pm 0.25$ cannot be distinguished from one another on this scale.
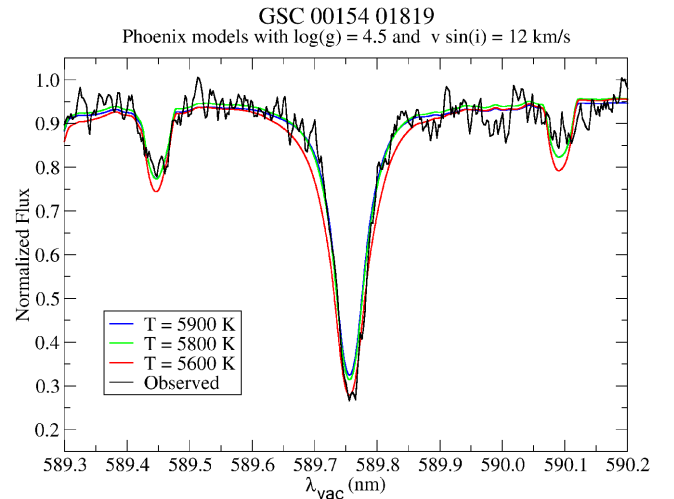

Figure 6. The spectrum of GSC 00154−01819 with telluric lines removed in the region of the Na D1 line compared to rotationally broadened PHOENIX models.

velocities the effect of different limb-darkening models is small, and Díaz et al. (2011) note that most authors use a fixed value of ϵ in their analyses of rotational broadening. After confirming that the effect of ϵ was not detectable, we also chose a fixed $\epsilon = 0.5$ and compared rotationally broadened PHOENIX spectra to the observational data. The best fit was for $v\sin(i) = 12.0 \pm 2$ km s^{-1}, which is to say a relatively slow rotator consistent with a late spectral type. Fig. 5 shows similar models compared to the observed spectrum with nearby pixels resampled and averaged to reduce noise.

The Na D, Mg b, Hα, and Hβ regions are sensitive to the spectral type and metallicity of the star. Figs 6 and 7 show the Na D lines with three different temperature model spectra, all with solar abundances and $v\sin(i) = 12.0$. It is clear from this that $T_{\mathrm{eff}} = 5800$ K is a representative temperature, but different regions of the line fit better than others. Nevertheless, the fit to the theoretical spectrum is remarkably good and the temperature is certainly $T_{\mathrm{eff}} = 5800 \pm 100$ K. Similarly, the Mg b region shown in Fig. 8 fits well for the same
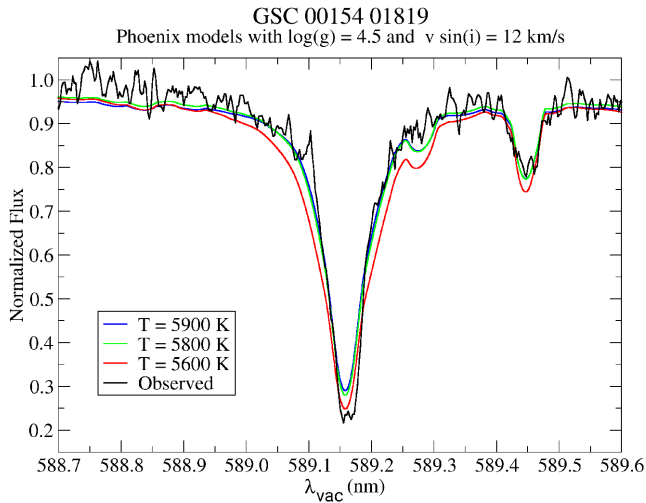
Figure 7. The spectrum of GSC 00154−01819 with telluric lines removed in the region of the Na D2 line compared to rotationally broadened PHOENIX models.
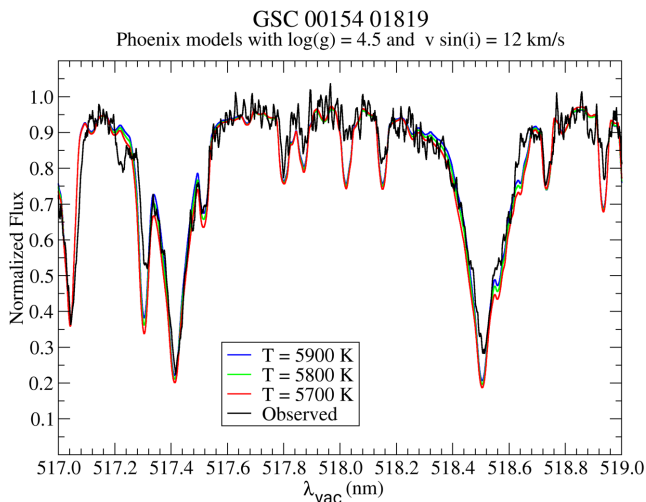

Figure 9. The spectrum of GSC 00154−01819 with telluric lines removed in the region of the H α line compared to rotationally broadened PHOENIX models. Emission on the red side of H α is from H I in the background Rosette nebula. The line at 657 nm is an Fe I $3d^7\,4p$–$4d$ transition missing in the PHOENIX models.

Figure 8. The spectrum of GSC 00154−01819 with telluric lines removed in the region of the Mg b lines compared to rotationally broadened PHOENIX models.
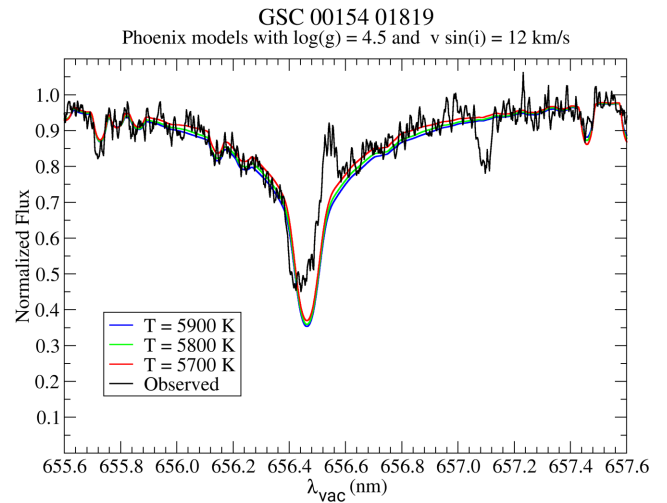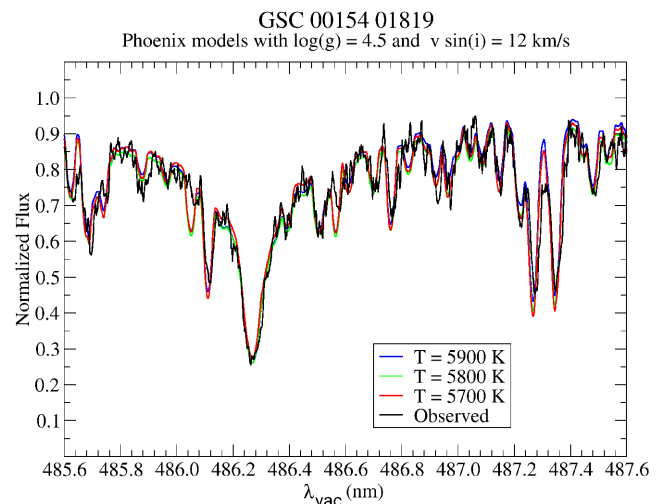

Figure 10. The spectrum of GSC 00154−01819 with telluric lines removed in the region of the H β line compared to rotationally broadened PHOENIX models.

temperature range. Similarly, Figs 9 and 10 show the first two lines of Balmer series and nearby Fe I lines. The H α spectrum also pieces of evidence an emission component which is not from the star, but from the Rosette nebula summed over the slit aperture. The nebular emission will be discussed in Section 9 after we first extract the radial velocity from a comparison of the model and observed stellar spectra.

7 RADIAL VELOCITY

The comparison with model stellar spectra was done in a geocentric reference frame, that is with the star's redshift due to its radial velocity removed. Given a precision wavelength calibration established from the telluric lines, and the identification of the star's temperature so that an accurate template is known, we can now find the apparent radial velocity of the star from the shift in the observed spectrum relative to the template. We used the PyAstronomy Library's crosscorrRV routine with the H α, Na D, and Mg b line region data as input to the template spectrum for $T_{\rm eff} = 5800$ K

(The PyA Group 2017). This routine maximizes the correlation, and returns a topocentric radial velocity of the observed star. The results are shown in Table 4.

These are the velocities between the telescope and the star at the moment of the observation. They include the rotation of the Earth, Earth's motion about the Solar system barycentre, and the star's motion relative to the barycentre. It is the later quantity that is of interest. The correction from topocentric to barycentric velocities is done with PyAstronomy Library's 'helcorr' routine (The PyA Group 2017). As input the routine requires the longitude, latitude, altitude, Julian date, and time of the observation. Also given the celestial coordinates of the target and the apparent topocentric radial velocity, it makes the geometrical and orbital computations to return the corresponding barycentric velocity. Taking each spectral region separately, we find a mean topocentric velocity of $29.2 \pm 1.99\,{\rm km\,s^{-1}}$. The result for a cross-correlation of the entire spectrum is similar, $30.77 \pm 1.99\,{\rm km\,s^{-1}}$. The correction to

Table 4. Radial velocity of GSC 00154−01819.

Topocentric radial velocity	
H α	27.91 km s^{-1}
Na D	28.24 km s^{-1}
Mg b	31.52 km s^{-1}
Mean of regions	29.2 ± 2.0 km s^{-1}
Complete spectrum	30.77 ± 1.99 km s^{-1}

Barycentric radial velocity	
Geocentric JD	2457 056.945 14
Heliocentric JD	2457 056.949 54
Target RA	97.990 641 68°
Target declination	4.963 797 222°
Barycentric velocity towards the star	−16.42 km s^{-1}
Topocentric	30.77 ± 1.99 km s^{-1}
Barycentric correction	−16.42 km s^{-1}
Barycentric radial velocity	+14.35 ± 1.99 km s^{-1}

Figure 11. The spectrum of GSC 00154−01819 with telluric lines removed in the region of the H α line compared to rotationally broadened solar spectrum.

Figure 12. The spectrum of GSC 00154−01819 with telluric lines removed in the region of the Na D lines compared to rotationally broadened solar spectrum.
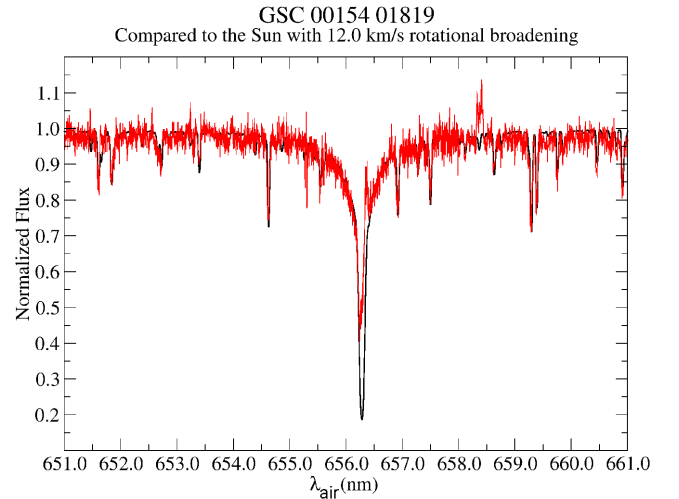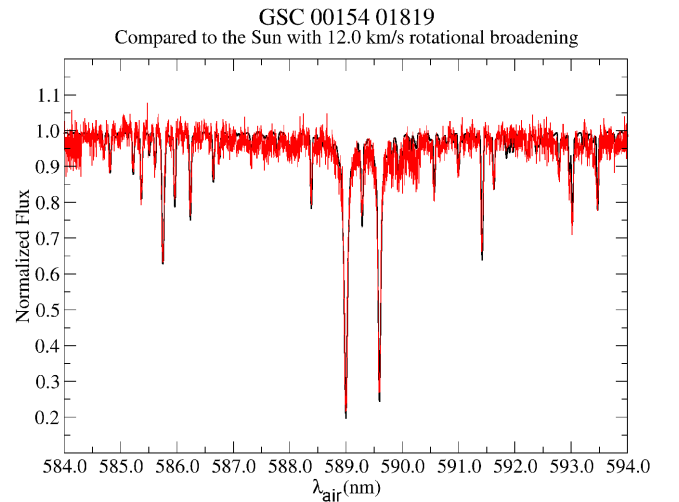
the barycentre is −16.42 km s^{-1}, resulting in a barycentric radial velocity of +14.4 ± 2.0 km s^{-1} for the entire spectrum, and slightly lower at +12.8 ± 2.0 km s^{-1} from the mean of the selected regions. HD 46150 identified in Fig. 2 as the bright star 1′25″ southwest of GSC 00154−01819 has a radial velocity of 31.83 ± 0.66 km s^{-1} (Wenger et al. 2000; Boyajian et al. 2007). The cluster NGC 2244 has a mean radial velocity of 26.16 ± 3.37 km s^{-1} (Wenger et al. 2000; Kharchenko et al. 2005). Thus the radial velocity alone establishes that the star is not a cluster member, and that it is also probably not inside the Rosette nebula.

8 NEW STELLAR DATA

The new spectroscopic data establish that GSC 00154−01819 is cooler, fainter, redder, and closer than we had anticipated based on the literature data shown in Table 2. The key piece of information is its effective temperature, 5800 ± 100 K. The PHOENIX models then provide the stellar mass, radius, and absolute luminosity. Pecaut & Mamajek (2013) have used new observational data and the PHOENIX models to assign $T_{\rm eff}$, intrinsic colours, and bolometric corrections to dwarf star spectral types O9 to M9, and based on that work we identify GSC 00154−01819 as spectral type G2V. Given its match to a spectrum with solar metallicity, it is a twin of the Sun. The weight of the spectral evidence is apparent in the data shown in Figs 11–13 which compare the stellar spectrum to the Kurucz et al. solar flux spectrum with telluric lines (Kurucz et al. 1984). The solar spectrum has been broadened with a 12 km s^{-1} rotation to simulate an integrated-disc observation of a distant star.

The equivalence of these spectra, and particularly the close match on spectral line shapes, confirms that this is a main-sequence G2V star. With the clear assignment of spectral type, we know the star's intrinsic colours and absolute magnitude, and thus the obscuration by the local interstellar medium and its distance.

The $v \sin(i) = 12$ km s^{-1} rotation derived from the width of the stellar lines is informative of the rotation period, even with an unknown inclination i. If $i = 90°$ and we are observing the star's equatorial velocity, the rotation period is $P = 2\pi R_\star / v$. For smaller inclinations as our view approaches pole-on, this apparent velocity is smaller than the equatorial velocity. Thus the assumption of an equatorial view gives the maximum P consistent with an observed $v \sin(i)$, that is

$$P_\star < 2\pi R_\star / v \sin(i). \tag{1}$$

In a study of rotation periods of stars in NGC 6819 using the long time base of Kepler mission data, Meibom et al. (2015) established a well-defined relationship between a star's rotation period (from milli-magnitude variation of its apparent magnitude), and its mass and colour at the age of the cluster. This is a refinement and confirmation of gyrochronology in which the age of a star is determined from a measurement of its rotation. In his review of the determination of the ages of stars, Soderblom (2010) concluded that for type G and K stars using the period $P_\star$ is one of the better methods available to determine a star's age. The method is tied to the spin-down of stars through the deterministic coupling of their magnetic fields to the plasma in the star's environment, that is, the age of a star of given type determines its rotation rate. Calibration of the relationship is through observations of clusters of known ages and theoretical models, and Soderblom recommends using the
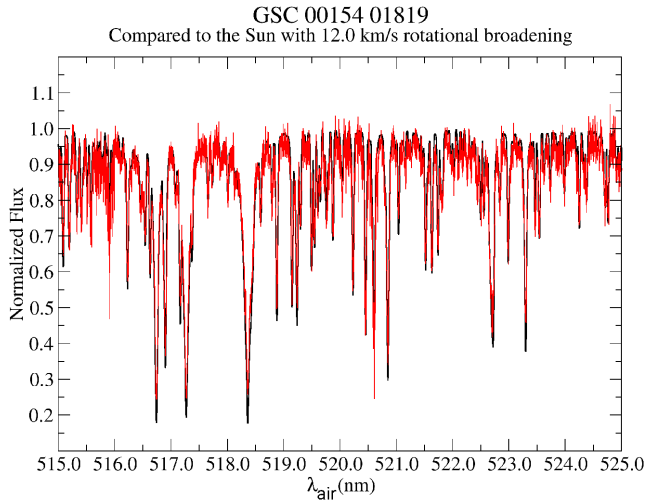
Figure 13. The spectrum of GSC 00154−01819 with telluric lines removed in the region of the Mg b lines compared to rotationally broadened solar spectrum.

work of Mamajek & Hillenbrand (2008) for F, G, and K stars. Similarly, the subsequent work of Meibom et al. (2015) concludes that gyrochronology can provide an accurate age, with the caveat that for the youngest stars with ages less than about 300 Myr there is a dispersion of rotation periods spanning two orders of magnitude. As stars age, the dispersion reduces rapidly and the gyrochronological ages converge by 600 Myr.

For a star of solar radius, an equatorial rotational velocity of $12\,\mathrm{km\,s^{-1}}$ implies a rotational period of 4.2 d for the star. This short period would be detectable by ground-based photometry of a spotted or chromospherically active star, but there are no confirming observations reported as yet. The Sun's slower differential rotation is well-established from observations of its spots, chromosphere, and corona, to have an equatorial sidereal period of 24.47 d. The long period and correspondingly slow surface velocity ($2.07\,\mathrm{km\,s^{-1}}$) are appropriate for its 4.6 billion year age. The much shorter period of GSC 00154−01819 is suggestive of youth. Indeed, fig. 1 of Meibom et al. shows a surface plot of the hypothetical relationship for period, age, and ($B − V$) colours of cool stars (Meibom et al. 2015). On that diagram, this star would have less than the 600 Myr gyrochronological age at which data are expected to be consistent. However, the calibration data given by Mamajek & Hillenbrand (2008) in their fig. 9 show that a star with a 4.2 d rotation period and solar colour would be in the same region as members of the Pleiades with an age of 130 Myr.

Mamajek and Hillenbrand provide the calibration relationship based on four parameters: a, b, c, and n.

$$P(B - V, t) = f(B - V)g(t) \qquad (2)$$

$$f(B - V) = a((B - V)_0 - c)^b \qquad (3)$$

$$g(t) = t^n \qquad (4)$$

For the age of the star t in millions of years, their revised gyrochronology parameters are $a = 0.407 \pm 0.021$, $b = 0.325 \pm 0.024$, $c = 0.495 \pm 0.010$, and $n = 0.566 \pm 0.008$. Thus there is a power-law relationship between period and age which is colour-dependent in the observational calibration, reflecting an initial mass-dependence

Table 5. New data on GSC 00154−01819.

Spatial parameters	
Right ascension	$06^\mathrm{h}31^\mathrm{m}57.754^\mathrm{s}$ ICRS (J2000)
Declination	$+04°57'49.67''$ ICRS (J2000)
Proper motion (RA)	3.412 ± 1.576 mas yr^{-1}
Proper motion (Dec.)	-13.231 ± 0.690 mas yr^{-1}
Parallax	4.5 mas
Distance	219 pc
Radial velocity	$+14.35 \pm 1.99$ km s^{-1}
Stellar parameters	
Effective temperature, T_eff	5800 K
Spectral type	G2V
Metallicity	Solar
Rotation, $v \sin(i)$	12 ± 2 km s^{-1}
Age	<180 My
Radius	6.512×10^5 km
Mass	2.01×10^{30} kg
Luminosity	3.42×10^{26} W
Absolute magnitude, M_V	4.862
V_C	11.565^a
$B_C - V_C$	0.620^a
R_C	11.01$^{a,\,b}$
R_C	11.1^b

^{a}Wenger et al. (2000)
$^b R_C \approx 11.1$ (this work suggested revision).

Table 6. GSC 00154−01819 colours.

	GSC 00154−01819 and G2V photometric colours		
Colour	Observed^a	BT-Settl model^b	Reference^c
$U_C - B_C$	0.145	0.201	0.133
$B_C - V_C$	0.620	0.674	0.650
$V_C - R_C$	0.465		0.363
$V_C - I$	0.715	0.726	0.713
$V_C - J$	1.156		1.197
$V_C - H$	1.434		1.491
$V_C - K$	1.489		1.564

^{a} Johnson–Cousins colours from Wenger et al. (2000).
^{b} Pecaut & Mamajek (2013), table 4 for $T_\mathrm{eff} = 5800$ K and $\log(g) = 4.5$ cm s^{-2}.
^{c} Pecaut & Mamajek (2013) table 5 and appendix C.

in the underlying physical stellar development. With these values for a solar colour $(B - V) = 0.65$, we find the star's age t is 180 Myr. Given P is an upper bound because of the unknown inclination i, the star's age from this method is also an upper bound.

The new observed and derived data are summarized in Tables 5 and 6. We note that the colours of the star match those of the G2V comparisons both in the BT-Settle model calculations based on the PHOENIX grid, and in the reference values recommended by Pecaut & Mamajek (2013) with one exception, the values of $V_C − R_C$. Given that V_C enters into the other near-IR and IR colours, it appears likely that it is the value of R_C that is in error, and that it should be about 0.1 mag higher than listed by Simbad from Wang et al.'s table 6 of available optical photometry (Wenger et al. 2000; Wang et al. 2008). Table 1 describes the sources of the data summarized by Wang, and it seems reasonable that there are unrecognized differences in the filters and data reductions of the various observers. A tentative revised value for R_C is indicated in Table 5. It does not bear on the following analysis. The value for $B_C − V_C$ is 0.03 bluer than both the Sun's reference colour and the models.
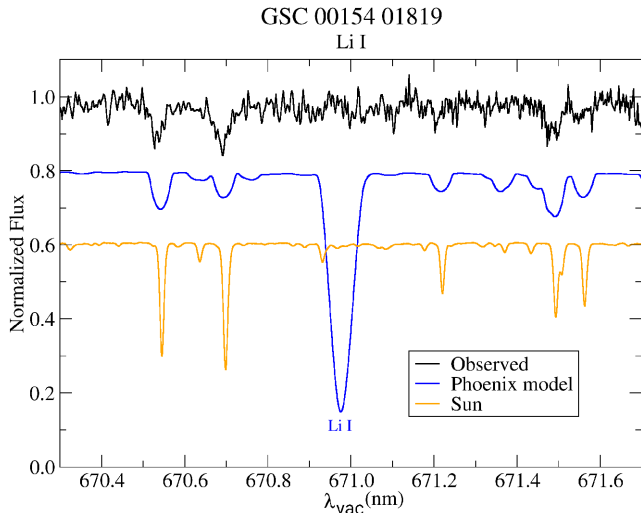
Figure 14. The spectrum of GSC 00154−01819 in the region of the Li I resonance line. The PHOENIX model includes Li with meteoritic abundance $\log \epsilon_{\text{Li}} = 3.26$ and clearly marks the wavelength expected. The absence of detectable Li in both the Sun and the target star is obvious.

These comparisons suggest that GSC 00154−01819 is not significantly reddened, which would imply that it is within the low-reddening volume of the Local Bubble (Lallement et al. 2003, 2014). However, Pecaut & Mamajek (2013) note that recently formed stars are either far away (i.e. in this instance within the Rosette), or still in their birth molecular cloud. With the assumption of no reddening, the apparent $m_V = 11.565$, may be compared to a reference absolute magnitude for this spectral type, $M_V = 4.862$, to establish a distance to the star. With a distance modulus of $m_V − M_V = 6.703$, the star is 219 pc or 715 light-years from the Sun. A corresponding parallax of 4.5 milliarcsec would have been detectable with *Hipparcos* but the star was not included in the catalogue so there is no confirming parallax measurement (Perryman et al. 1997). Parallaxes from the *Gaia* spacecraft, anticipated in 2018 April, will provide further context (Gaia Collaboration 2016). Since we use the absolute magnitude for a G2V solar star for finding the distance, it follows that the bolometric magnitude should be the same as the Sun, $M_{\text{bol}} = 4.7554$. The luminosity given in Table 5 is from the PHOENIX model for a 5800 K star and is 11 per cent lower than the solar luminosity of 3.8270×10^{26} W.

We note that because the star is not significantly reddened and is young, it is close to the zero-age main sequence and its spectrum should match that of the PHOENIX models closely. This is borne out by the selected detailed comparisons shown here. Therefore, the spectral energy distribution (SED) of the star is known well enough for it to serve for flux calibration both for stellar photometry, and for wide field nebular mapping when the filter passbands used for those measurements are known. Although the spectra which were taken were not independently flux calibrated, the PHOENIX model also allows a relative flux calibration of the AAT spectral data so that line ratios of the background emission nebula can be found.

Given the apparent youth of this star, its lithium abundance would be of interest. Fig. 14 compares the Li resonance line region observed with the PHOENIX model and the Sun. Lithium is not detectable in the star to the level of the noise. Recently, Beck et al. (2017) considered the relationship of Li abundances and rotation for solar analogues. Fig. 2 of that paper has spectra of the solar-like stars they selected from the Kepler catalogue for which Li abundance could be measured. GSC 00154−01819 would fall at

the bottom of their scale, with the Sun having a Li abundance too small to create a measurable resonance line at 670.8 nm. On their dex scale, relative to H the abundance $\log \epsilon_{\text{Li}} = \log (n_{\text{Li}}/n_{\text{H}}) + 12$ would be $\sim < 1.5$

Beck et al. (2017) found a correlation of Li abundance with stellar rotation taken as an indicator of age. On their rotation plot, with a period of 4.2 d and $v \sin i = 12 \, \text{km s}^{-1}$, this star is at the extreme of their scale based on older stars in the Kepler field. The low Li abundance and fast rotation seen in this case are not consistent with the relationship between Li abundance and rotation that they found.

Baumann et al. (2010) have studied lithium abundance in solar-like stars, looking for a relationship between those known to have planets and those without. They concluded that lithium versus age trends were statistically the same whether planets were known or not. They found strong trends in Li abundance with T_{eff} from a low of less than $\log \epsilon_{\text{Li}} = 0.5$ at 5700 K to 2.5 at 5900 K. The value we found of <1.5 is consistent with their distribution at 5800 K. They also found an age trend, with $\log \epsilon_{\text{Li}}$ increasing for younger stars up to more than 2.5 for stars under 2 Gyr age, but with a very large uncertainty in age that makes the correlation imprecise. For solar twins in open clusters with solar metallicity, stars with less than 1 Gyr age all have $\log \epsilon_{\text{Li}} \sim >2.0$, though the range between a few Myr and 1 Gyr is undersampled in their fig. 3. Their analysis of observational data was in agreement with values predicted from models with different initial rotational velocities, and also exhibited a clearer trend for metal-rich solar analogues.

As noted by Baumann et al. (2010), the Sun's Li abundance is low compared to many nearby solar analogues and to the abundance of Li in meteorites. Fig. 14 shows the model spectrum based on meteoritic Li abundance, and it is qualitatively clear that the star has an abundance of the same low order as the Sun. Depletion of Li in the Sun is attributed to its age, and to its planetary system. Oddly, in contrast to their survey and to that of Beck et al. (2017), this star is rotating rapidly and is presumed to be young, yet it shows depleted Li. Since other abundances in the star track those in the Sun, the depletion of Li in this young solar analogue suggests there is a mechanism in addition to age at work. If the star has a dust disc, a possibility indicated by the SED in the infrared, planet formation may be one of those.

9 NEBULAR SPECTRUM

The spectra which were taken at the AAT record not only the star and the transmission spectrum of Earth's atmosphere as we have discussed, but also emission from Earth's atmosphere (airglow), and emission from the Rosette nebula. These emission features are easily distinguished in the original FITS spectral images because they extend beyond the seeing disc of the star. While Balmer emission would be possible in some stars and appear within the stellar PSF, the spatial dimension of the spectra allows us to identify that the emission contributions we detect are non-stellar. Furthermore, atmospheric emission lines are very narrow, while those from the nebula are broadened by differential motions along the line of sight. Fig. 15 shows the Hα region of one FITS science image. The spectrum extracted from all of the images is seen in Fig. 9.

Table 7 lists the brighter emission lines that should be in the Rosette spectrum, and the three bright forbidden night sky lines of [O I] that serve as benchmarks for emission detection. The table does not list numerous lines of OH which are present at longer wavelengths because the spectra that were processed through the USQ pipeline did not include the low orders above 7000 Å.
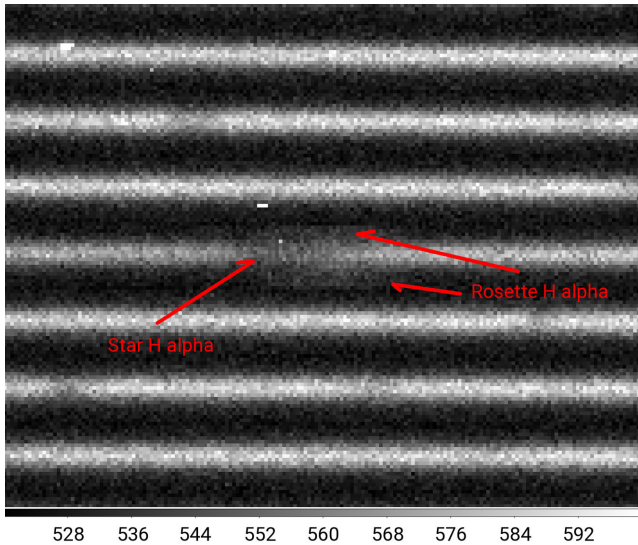
Figure 15. An unprocessed echelle spectrum of GSC 00154−01819. FITS science image 23 has been rotated 90° and transposed so that dispersion is horizontal with wavelength increasing to the right. Higher orders (longer wavelength) are at the top. The region around the Hα line in the 87th order is shown. The vertical dimension is angular displacement from the star, and the background Rosette nebula contributes at a greater radial velocity than the star's.

Table 7. Potential emission lines in the spectrum of GSC 00154−01819.

Potential Rosette nebula emission lines[a, b]	
Source	Rest λ_{air} (Å)
He I	7065.28
[S II]	6730.82
[S II]	6716.44
He I	6678.15
[N II]	6583.45
Hα	6562.801
[N II]	6548.05
He I	5875.67
[O III]	5006.843
[O III]	4958.911
He I	4921.93
Hβ	4861.363
Selected atomic airglow lines[a, c]	
Source	Rest λ_{air} (Å)
[O I]	6363.78
[O I]	6300.304
[O I]	5577.338

[a]Osterbrock et al. (1996).
[b]SDSS (2015).
[c]Chamberlain (1961).

Because these are high-resolution spectra, the signal/pixel is low and the possible useful data are limited to the few bright emission lines that are given in Table 7. To better identify lines of interest and confirm features that appear in the spectral plots, we re-processed the original FITS files through our own pipeline using ALSVID, the PYTHON routines that were developed during this work (Kielkopf, Collins & Huber 2017). Bias and flat frames were co-added with a median algorithm to eliminate cosmic ray events. The flat frames, which are spectra of a hot tungsten filament in a quartz envelope, were also bias subtracted and normalized. They reveal the
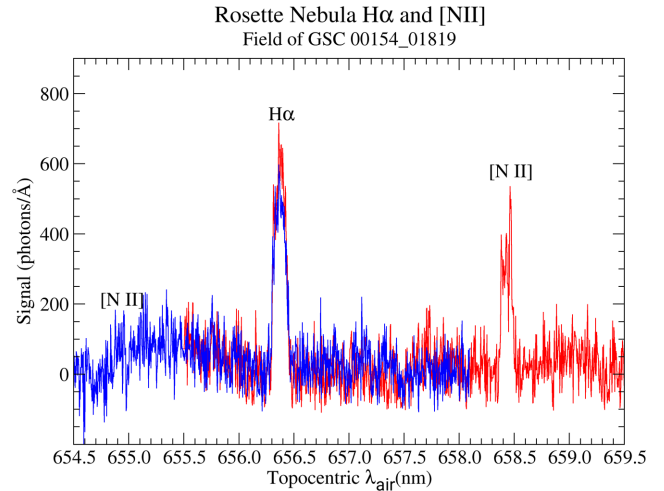

Figure 16. Hα and [N II] in the Rosette nebula behind the foreground star GSC 00154−01819. Wavelengths shown are in air for the date and time of observation, calibrated by Telfit. The signal shown is for an effective aperture of 0.32 arcsec^2 with a total of 3600 s exposure time.

interference fringing that affects spectra in very high orders, and also help to define the limits of the aperture mask that separates orders. Science frames are bias subtracted, and then co-added as sums to get the most data from the faint star. Co-adding in this way leaves the cosmic ray events and uncorrected bright pixels in the final data, but they can be selectively removed for the lines of interest. Correction for flats can introduce a gradient (the tungsten lamp is much cooler than the star) and also add pattern noise. In low-flux spectra the primary uncertainty in flux at any pixel is the shot noise in the statistics of the detected photons, that is $\pm\sqrt{N}$ where N is the number of detected photons. At an system gain of 1.3 photons per analog-to-digital unit (ADU), a digital 'count' of 100 ADU is equivalent to 130 photons, with an uncertainty of ±11. At this noise level, flat-field correction is not helpful and except for identifying orders we used only bias-subtracted spectra.

For each order of interest, the spectrum was rotated using spline interpolation so that select order ran parallel to a row, and rows sampling the star and the sky to either side were extracted and summed. These data for sky and star were then combined with the Telfit-calibrated spectra to confirm the identity, wavelength, and radial velocity of the features. The procedure introduces a wavelength uncertainty because the calibration must be transferred from the Telfit-processed stellar spectrum that runs through the centre of the aperture to the nebular spectrum that is offset above and below centre. The spectral lines in the echelle spectra are not precisely normal to the direction of dispersion, that is, they tilt slightly by an amount that increases with decreasing wavelength. This introduces a systematic error in addition to the uncertainty of matching the spectra which we estimate to be ±1 pixel in the dispersion direction, or about ±0.037 Å. That would be equivalent to $\pm1.7\,\mathrm{km\,s^{-1}}$ in velocity.

Fig. 16 shows Hα and the stronger [N II] line at 6583 Å. The [N II] line at 6548 Å may also be discernible above noise, but there is a baseline that varies because of contamination of the stellar continuum and fitting this line would not yield useful data. The baseline in the figure has been adjusted to remove a uniform background by subtracting a fifth-order polynomial fit to the envelope and it works well for the regions under the primary lines. Gaussian fitting to these lines will also remove remaining background, so that

the initial background removal is essentially cosmetic. Both strong lines are redshifted because of the Rosette's radial velocity, and are broadened by differential structure within the spatial aperture. The signals could be quantitatively compared to the stellar continuum, but we do not know the stellar PSF and the light losses associated with that, so the resulting absolute calibration would be uncertain to a factor of 2 or more. In this instance, difference in instrumental response between [N II] at Hα is not significant. For other lines, instrumental response can be removed by using the stellar continuum and the PHOENIX model standard. Values shown in the figure are summed over three 1200 s exposures for a total of 3600 s. The spectrograph slit has a projected width on the sky of about 1 arcsec, and each pixel in the camera focal plane accepts 0.32 arcsec perpendicular to the dispersion direction. Consequently, the values are for an effective aperture of 0.32 arcsec^2 wide. However, with 1.5 arcsec seeing and only about 5 pixels useful to either side of the stellar spectrum, the data are also averaged over a spatial region of the order of 3 arcsec^2 for each spectral data point.

Fitting for the Hα profile in the effective 3600 s total exposure with 0.32 arcsec^2 spatial integration gives a topocentric radial velocity derived from these data for the Rosette that is $42.38 \pm 0.49\,\mathrm{km\,s^{-1}}$, with a $1/e$ velocity dispersion of $31.59 \pm 0.70\,\mathrm{km\,s^{-1}}$ (or full width at half-maximum of $61.94 \pm 1.38\,\mathrm{km\,s^{-1}}$). For the epoch of these observations the correction to be added to topocentric radial velocity to have barycentric velocity is $-16.418\,\mathrm{km\,s^{-1}}$, giving a barycentric radial velocity for the gas of $25.96 \pm 0.49\,\mathrm{km\,s^{-1}}$. The uncertainty given is for the fitting, to which for radial velocity we must add the uncertainty in wavelength calibration of $\pm1.7\,\mathrm{km\,s^{-1}}$. Therefore the barycentric Hα radial velocity is $26.0 \pm 2.4\,\mathrm{km\,s^{-1}}$. This radial velocity is consistent with measurements of the whole nebula from the Wisconsin Hα Mapper Haffner et al. (2003). The width and radial velocity are in agreement with values given from selected regions of the Rosette by Smith (1973) using Fabry–Perot measurements, and of full widths of the order of $60\,\mathrm{km\,s^{-1}}$ measured by Fountain, Gary & Odell (1979) near the centre of the Rosette using an echelle.

Fitting the stronger [N II] line and given the precise rest wavelength from the SDSS table (SDSS 2015) as 6583.45 Å, the topocentric radial velocity is $41.3\,\mathrm{km\,s^{-1}}$ and the barycentric velocity is $24.9 \pm 2.8\,\mathrm{km\,s^{-1}}$ with the uncertainty in the wavelength calibration added to the uncertainty in the fitting as we did for Hα. The [N II] $1/e$ velocity dispersion is $28.3 \pm 1.6\,\mathrm{km\,s^{-1}}$ (full width at half-maximum of $55.5 \pm 3.2\,\mathrm{km\,s^{-1}}$). Therefore, the values of the radial velocity and the gas velocity dispersion for [N II] are close to those for Hα when measurement errors are taken into account. The ratio of flux in photons is $S([\mathrm{N\,II}])/S(\mathrm{H}\alpha) = 0.56 \pm 0.08$ given negligible change in instrument response over this wavelength range.

There is also a small but detectable signal in [S II] in the red, and in Hβ in the blue. For other lines in Table 7 the nebular emission is lost in the stellar scattered light and the sky background. The rest air wavelength of Hβ is 4861.363 Å, yielding a rather large barycentric radial velocity of $42.1 \pm 6.4\,\mathrm{km\,s^{-1}}$ after a wavelength calibration uncertainty of 2 pixels is included. The Hβ $1/e$ velocity dispersion is $20.7 \pm 4.4\,\mathrm{km\,s^{-1}}$ (full width at half-maximum of $40.6 \pm 8.6\,\mathrm{km\,s^{-1}}$).

The total flux detected at Hβ in this spatial area can be compared to Hα if we take into account the instrumental response ratio over this wavelength range. For this, we can use the stellar flux itself because our data show that the star is not reddened. We have the PHOENIX model of the star's flux, and we can compare the same spatial cross-section of the PSF at wavelengths near the Hβ and Hα lines. In this case, the stellar model ratio is $F_\star(\mathrm{H}\beta)/F_\star(\mathrm{H}\alpha) = 1.39$

Table 8. Rosette nebula background at GSC 00154−01819.

line	V_R (km s^{-1})[a]	σ_V (km s^{-1})[b]	Relative flux[c]
[S II] 6730.82 Å	26.702 ± 4.05	55.1 ± 11.2	0.114 ± 0.048
[S II] 6716.44 Å	31.3 ± 2.33	39.2 ± 6.4	0.122 ± 0.043
[N II] 6583.45 Å	24.9 ± 2.8	55.5 ± 3.2	0.56 ± 0.08
[N II] 6548.05 Å	–	–	–
Hα 6562.801 Å	26.0 ± 2.4	61.94 ± 1.38	1.0
Hβ 4861.363 Å	42.1 ± 6.4	40.6 ± 8.6	0.261 ± 0.113

[a]Barycentric radial velocity V_R.
[b]HWHM velocity dispersion σ_V.
[c]Flux in photons relative to Hα.

in the continuum on the short wavelength side of both lines when the flux is measured in ergs s^{-1} cm^{-2} Å^{-1} at the star's surface. Measured in photons rather than in energy ($h\nu$), we must multiply this by $\lambda(\mathrm{H}\beta)/\lambda(\mathrm{H}\alpha)$ since it takes fewer photons at Hβ to have the equivalent energy at Hα. Thus the flux ratio in photons leaving the star is $F_\star(\mathrm{H}\beta)/F_\star(\mathrm{H}\alpha) = 1.03$. The measured continuum ratio in the UCLES data is $C_\star(\mathrm{H}\beta)/C_\star(\mathrm{H}\alpha) = 0.534$ when the same aperture is used on both echelle orders. Consequently, the instrument is less responsive at Hβ than at Hα by $0.534/1.03 = 0.518$. With this calibration, the emission line ratio for the Balmer series in the Rosette is $S(\mathrm{H}\beta)/S(\mathrm{H}\alpha) = (101.1/746)/0.518 = 0.261 \pm 0.113$. Or, the inverse ratio in photons is $S(\mathrm{H}\alpha)/S(\mathrm{H}\beta) = 3.8 \pm 1.7$. The uncertainty in the ratio is large primarily because of the noise in the measurement of the faint Hβ emission line profile. Similarly, we follow the same procedure for the two [S II] lines recorded in the spectra.

The spectroscopic properties of the nebula background close enough to the star to be seen in the slit are summarized in Table 8. The weaker [N II] was not measurable and is probably less than 20 per cent the strength of the stronger 6583 line.

10 SPECTRAL ENERGY DISTRIBUTION

The position of GSC 00154−01819 has been identified as a point source of interest in the 2MASS and WISE data bases, as well as the GSC. A search of the available catalogues using the VizieR 'Photometry Viewer' returned 110 entries within a 1 arcsec radius (Simon & Boch 2017). These data together provide a comprehensive SED for the star, and perhaps for its background nebula which is shown in Fig. 17. While we have excluded other nearby sample points that appear to primarily detect line of sight nebular emission, we have included the WISE3 and WISE4 data above 10 μm which are coincident with the stellar location. Based on WISE photometry of nearby regions in these same bands, however, it is clear that emission from the anomalous ridge feature is contributing significantly to the plotted flux above 10 μm. Those data points therefore are an upperbound to the stellar emission.

Also in the figure, the SEDs for the Sun (Cox 2000) and for the PHOENIX 5800 K model are shown as they would be detected at 200 pc in the absence of interstellar absorption. The agreement of the SED's supports our identification of this star as a nearby solar twin and the distance scaling to about 200 pc is clearly appropriate.

The data at the longest wavelengths may be interpreted in two ways. The most likely explanation of the anomalously large flux is that at these wavelengths the star's emission is lost in a much larger contribution from the nebula as we noted above. This possibility is made more apparent when images of the region in Hα and the WISE W4 bands are compared as in Fig. 1. The nebula is brightest
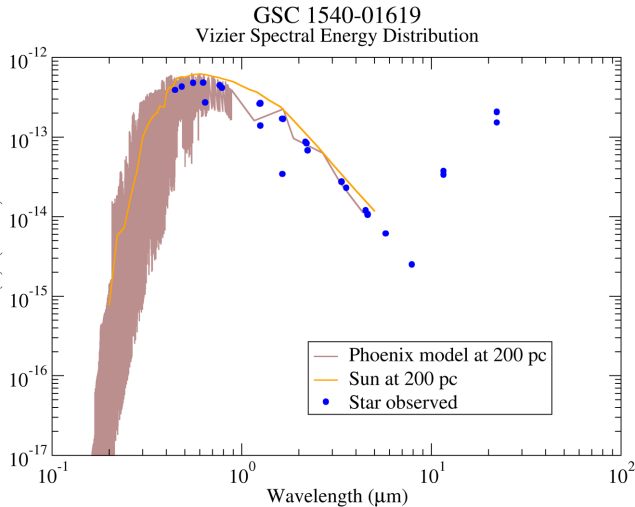
GSC 1540-01619
Vizier Spectral Energy Distribution

Figure 17. The SED of GSC 00154−01819 including data from the GSC, 2MASS, and WISE catalogues based on a search with the Vizier photometry viewer tool (Simon & Boch 2017). The solar and PHOENIX model spectra as they would be seen at 200 pc are overplotted for comparison.

in the W4 band, and there is little indication of a star in this image. In H α there is no hint of a nebula. However, the SED does not exclude the possibility that emission from a spatially unresolved disc is a component of the signal shown for wavelengths above 10 µm in Fig. 17. The infrared excess in this spectrum is remarkably similar to that identified as disc debris around other young stars and that suggests post-protoplanetary dust (Cotten & Song 2016; Binks & Jeffries 2017). Robitaille (2017) provides a set of synthetic SEDs suitable for Bayesian analyses of the inverse problem, determining the nature of the star and its environment from the observed spectrum. While focused on very young (<10 Myr) stars for which the background contributions can be identified and removed, the comprehensive synthetic samples inform about the effects of ambient medium, disc, envelope, and viewing angle on the observed spectrum. They show that the emission above 10 µm could arise from any of these components at the expense of energy radiated at shorter wavelengths. In order for a relatively unreddened stellar spectrum to be present, the synthetic SEDs would favour a face-on view of the debris disc. However, given the uncertainty in background removal, infrared spectroscopy with high spatial resolution separating the Rosette background from the stellar emission would be needed to settle this question and yield a reliable quantitative assessment of the disc mass.

11 CONCLUSIONS

Using the University College of London Echelle Spectrograph on the Anglo Australian Telescope, we have acquired high-resolution spectra of the 12th magnitude star GSC 00154−01819 near the apparent centre of the Rosette nebula. This target was selected with the intention of conducting absorption line spectroscopy along the line of sight to the nebula, based on recent cluster membership studies. These studies had suggested a reddened type A star embedded in the central cluster of the Rosette nebula, NGC 2244.

The observed high-resolution visible spectrum and a low-resolution SED from archival data were compared to the PHOENIX library of model spectra (Husser et al. 2013) to reveal that this star is actually an unreddened type G2V star with an effective surface temperature of 5800 ± 100 K. The barycentric radial velocity of the

star was found to be $14.4 \pm 2.0 \, \mathrm{km \, s^{-1}}$, while Doppler line broadening results from an implied equatorial rotational rate of at least $12 \, \mathrm{km \, s^{-1}}$. This rate, along with the spectral type, and gyrochronological parameters establishes an age estimate of only 180 Myr. The apparent lack of reddening for a G2V star also implies a distance of 219 pc. Thus the presumption that the star is in the Rosette Cluster is disproved, and in actuality it is a newly recognized nearby young solar analogue.

Emission from the background nebula has allowed an analysis of the radial velocity, dispersion, and relative strength of optical lines in the gas at the centre of the Rosette nebula. The calculated barycentric radial velocity of $25.96 \pm 0.49 \, \mathrm{km \, s^{-1}}$ for the H α line were consistent with past studies at this wavelength, while velocity dispersion estimates in H α, H β, [N II], [O III], and [S II] provide kinematic details of the line-of-sight gas velocity structure with $\sigma_{\mathrm{H}\alpha} = 61.94 \pm 1.38$ that were not previously available at this spatial resolution.

An infrared excess emission at wavelengths above 10 µm is apparent in WISE data for this object. While the emission likely comes from the anomalous ridge feature that instigated this investigation, if there is a significant contribution from the star it would indicate a post-planetary debris disc such as has been recently noted for other young stars.

REFERENCES

ADS 2017, The SAO/NASA Astrophysics Data System. Available at: http://adswww.harvard.edu/

Baumann P., Ramírez I., Meléndez J., Asplund M., Lind K., 2010, A&A, 519, A87

Beck P. G. et al., 2017, A&A, 602, A63

Berghöfer T. W., Christian D. J., 2002, A&A, 384, 890

Binks A. S., Jeffries R. D., 2017, MNRAS, 469, 579

Boyajian T. S. et al., 2007, PASP, 119, 742

Carroll J. A., 1933, MNRAS, 93, 478

Castelli F., Kurucz R. L., 2003, in Piskunov N., Weiss W. W., Gray D. F., eds, Proc. IAU Symp. 210, Modelling of Stellar Atmospheres. Astron. Soc, Pac., San Francisco, CA, p. 20

Chamberlain J. W., 1961, Physics of the Aurora and Airglow. Academic Press, New York

Chen L., de Grijs R., Zhao J. L., 2007, AJ, 134, 1368

Clough S. A., Iacono M. J., Moncet J.-L., 2014, Astrophysics Source Code Library, record ascl:1405.001

Collins G. W., II, Truax R. J., 1995, ApJ, 439, 860

Cotten T. H., Song I., 2016, ApJS, 225, 15

Cox A. N., 2000, Allen's Astrophysical Quantities. Springer-Verlag, New York

Díaz C. G., González J. F., Levato H., Grosso M., 2011, A&A, 531, A143

Diego F., Charalambous A., Fish A. C., Walker D. D., 1990, in Crawford D. L., ed., Proc. SPIE Conf. Ser. Vol. 1235, Instrumentation in Astronomy VII. SPIE, Bellingham, p. 562

Donati J.-F., Semel M., Carter B. D., Rees D. E., Collier Cameron A., 1997, MNRAS, 291, 658

Edlén B., 1966, Metrologia, 2, 71

ESO 2015, ESO ScienceArchive. Available at: http://archive.eso.org/eso/eso_archive_main.html

ESO 2017, Thorium-Argon Atlas. Available at: http://www.eso.org/sci/facilities/paranal/instruments/uves/tools/tharatlas.html

Ferland G. J. et al., 2017, Rev. Mex. Astron. Astrofis., 53, 385

Fountain W. F., Gary G. A., Odell C. R., 1979, ApJ, 229, 971

Gaia Collaboration, 2016, A&A, 595

Gordon I., Rothman L. S., Wilzewski J. S., Kochanov R. V., Hill C., Tan Y., Wcislo P., 2016, AAS/Division for Planetary Sciences Meeting Abstracts. p. 421.13. Available at: https://aas.org/files/dps-epsc-abstract-book-final.pdf

Gray D. F., 2008, The Observation and Analysis of Stellar Photospheres. Cambridge Univ. Press, Cambridge

Gullikson K., Dodson-Robinson S., Kraus A., 2014, AJ, 148, 53

Haffner L. M., Reynolds R. J., Tufte S. L., Madsen G. J., Jaehnig K. P., Percival J. W., 2003, ApJS, 149, 405

Hensberge H., Vrancken M., Verschueren W., 1998, A&A, 339, 141

Hensberge H., Pavlovski K., Verschueren W., 2000, A&A, 358, 553

Husser T.-O., Wende-von Berg S., Dreizler S., Homeier D., Reiners A., Barman T., Hauschildt P. H., 2013, A&A, 553, A6

Johnson H. L., 1962, ApJ, 136, 1135

Kharchenko N. V., Piskunov A. E., Röser S., Schilbach E., Scholz R.-D., 2005, A&A, 438, 1163

Kielkopf J. F., Collins K., Huber J., 2017, ALSVID: Algorithms for Visualization and Processing of Image Data. Available at: http://www.astro.louisville.edu/software/alsvid/index.html

Kraemer K. E., Shipman R. F., Price S. D., Mizuno D. R., Kuchar T., Carey S. J., 2003, AJ, 126, 1423

Krełowski J., Galazutdinov G., Kołos R., 2011, ApJ, 735, 124

Kurucz R. L., 1970, SAO Special Report, 309

Kurucz R. L., Furenlid I., Brault J., Testerman L., 1984, Solar Flux Atlas from 296 nm to 1300 nm, NSO Atlas No. 1. Available at: ftp://vso.nso.edu/pub/atlas/fluxatl

Lallement R., Welsh B. Y., Vergely J. L., Crifo F., Sfeir D., 2003, A&A, 411, 447

Lallement R., Vergely J.-L., Valette B., Puspitarini L., Eyer L., Casagrande L., 2014, A&A, 561, A91

Lovis C., Pepe F., 2007, A&A, 468, 1115

Mamajek E., 2015, Basic Astronomical Data for the Sun. Available at: https://sites.google.com/site/mamajeksstarnotes/basic-astronomical-data-for-the-sun

Mamajek E. E., Hillenbrand L. A., 2008, ApJ, 687, 1264

Meibom S., Barnes S. A., Platais I., Gilliland R. L., Latham D. W., Mathieu R. D., 2015, Nature, 517, 589

Morton D. C., 1991, ApJS, 77, 119

Murphy M. T., Tzanavaris P., Webb J. K., Lovis C., 2007, MNRAS, 378, 221

Ogura K., Ishida K., 1981, PASJ, 33, 149

Osterbrock D. E., Fulbright J. P., Martel A. R., Keane M. J., Trager S. C., Basri G., 1996, PASP, 108, 277

Palmer B. A., Engleman R., 1983, Technical Report LA-9615, Atlas of the Thorium Spectrum. Lawrence Livermore National Laboratory

Park B.-G., Sung H., 2002, AJ, 123, 892

Pecaut M. J., Mamajek E. E., 2013, ApJS, 208, 9

Perryman M. A. C. et al., 1997, A&A, 323, L49

Reiners A., Schmitt J. H. M. M., 2002, A&A, 384, 155

Robitaille T. P., 2017, A&A, 600, A11

Román-Zúñiga C. G., Lada E. A., 2008a, preprint (arXiv: Astrophysics e-prints)

Román-Zúñiga C. G., Lada E. A., 2008b, Star Formation in the Rosette Complex. Astronomical Society of the Pacific Monograph Publications, San Francisco, p. 928

Ryder S., 2000, UCLES Thorium-Argon Atlas with the MITLL CCD

Sbordone L., Bonifacio P., Castelli F., Kurucz R. L., 2004, Mem. Soc. Astron. Ital. Suppl., 5, 93

SDSS 2015, Sloan Digital Sky Survey Vacuum Wavelengths. Available at: http://classic.sdss.org/dr7/products/spectra/vacwavelength.html

Simon A.-C., Boch T., 2017, VizieR Photometry Tool, http://vizier.u-strasbg.fr/vizier/sed/

Smith M. G., 1973, ApJ, 182, 111

Soderblom D. R., 2010, Annu. Rev. Astron. Astrophys., 48, 581

The PyA Group 2017, PyAstronomy Library. Available at: http://www.hs.uni-hamburg.de/DE/Ins/Per/Czesla/PyA/PyA/index.html

Tinney C. G., Butler R. P., Marcy G. W., Jones H. R. A., Penny A. J., Vogt S. S., Apps K., Henry G. W., 2001, ApJ, 551, 507

van Schewick H., 1958, Veroeffentlichungen des Astronomisches Institute der Universitaet Bonn, 51, 1

Verschueren W., 1991, PhD thesis, Vrije Universiteit Brussel (VUB)

Walker G. A. H., 1963, MNRAS, 125, 141

Wang J., Townsley L. K., Feigelson E. D., Broos P. S., Getman K. V., Román-Zúñiga C. G., Lada E., 2008, ApJ, 675, 464

Wenger M. et al., 2000, A&AS, 143, 9

Weselak T., Galazutdinov G. A., Musaev F. A., Krełowski J., 2008, A&A, 484, 381

Wright D. 2015, Anglo-Australian Telescope UCLES. Available at: https://www.aao.gov.au/science/instruments/current/ucles/overview

This paper has been typeset from a TEX/LATEX file prepared by the author.